PERGAMON

International Journal of Multiphase Flow 27 (2001) 2105–2127

International Journal of Multiphase Flow

www.elsevier.com/locate/ijmulflow

Visualisation and modelling studies of churn flow in a vertical pipe

J.R. Barbosa Jr., A.H. Govan [1], G.F. Hewitt *

Department of Chemical Engineering and Chemical Technology, Imperial College of Science, Technology and Medicine, Prince Consort Road, London SW7 2BY, UK

Received 24 November 1999; received in revised form 3 July 2001

Abstract

Churn flow is an important flow regime intermediate between slug flow and annular flow. A feature of this regime is the occurrence of very large waves travelling upwards over a liquid film substrate which may intermittently travel downwards. These waves are often formed close to the liquid inlet where their behaviour is usually difficult to observe. This paper describes a series of experiments using a test section with a specially constructed transparent liquid inlet. High-speed video recordings show clearly the process of wave formation and analysis of the recordings gave data on wave frequencies and typical velocities. Also, predictions of velocity and distance travelled by the waves were obtained via the application of a simple mathematical model that takes into account the forces acting on a circumferentially coherent wave.

Keywords: Gas–liquid flow; Churn flow; Annular flow; Visualisation; Wave motion

1. Introduction

This paper is concerned with the *churn flow* regime in vertical gas–liquid flow. Here, we define churn flow as a regime which occurs after the breakdown of *slug flow* as velocity and/or quality increase. In churn flow, the large Taylor bubbles characteristic of slug flow have disappeared but, when churn flow is viewed from the outside through a transparent tube, characteristic reversals in flow velocity are observed. This regime has been given the name churn flow for many decades

* Corresponding author. Tel.: +44-20-759-45562; fax: +44-20-759-45564.
E-mail address: g.hewitt@ic.ac.uk (G.F. Hewitt).
[1] Present address. Petroleum Development Division, ADMA-OPCO, PO Box 303, Abu Dhabi, United Arab Emirates.

0301-9322/01/$ - see front matter
PII: S0301-9322(01)00048-9

(Hewitt and Hall-Taylor, 1970) but its detailed characteristics have not been widely investigated, despite the fact that the regime occurs over a relatively large range of flow conditions. Some confusion has been caused in the literature by the term 'churn' being used in at least two other contexts:

1. The 'churn turbulent' bubbly flow regime as defined, for instance, by Zuber and Findlay (1965). Essentially, this regime is delineated to allow specific forms of the drift-flux model to be used over certain ranges of gas and liquid velocity.
2. The churn flow regime defined by Taitel et al. (1980). This was seen as a form of developing slug flow; the longer the pipe, the more likely the flow was to correspond to classical slug (or plug) flow rather than to a flow with apparently churning motion which was defined, in this case, as the churn flow regime.

We believe it appropriate to retain the older designation of churn flow as an important regime occurring between slug flow and annular flow.

Visualisation studies by Hewitt et al. (1985) reveal the nature of the churn flow regime. Essentially, it has similarities to annular flow in that there is a continuous gas core in the centre of the channel and a liquid layer near the channel wall. Nicklin and Davidson (1962) used the alternative name 'semi-annular' flow which also recognised the often annular nature of the churn flow regime. However, we believe strongly that it is important to make a distinction between annular flow and churn flow since its characteristics are so very different. The characteristics which distinguish it from annular flow are as follows:

1. The breakdown of slug flow is accompanied by a very rapid increase in pressure gradient due to intensified wave activity and friction. This is well illustrated by the pressure gradient data obtained by Owen (1986), an example which is shown in Fig. 1. In this figure, U_G^* is the dimensionless gas velocity given by,

$$U_G^* = U_G \left[\frac{\rho_G}{g d_T (\rho_L - \rho_G)} \right]^{1/2}, \tag{1}$$

where U_G is the gas superficial velocity, g is the acceleration due to gravity, d_T is the diameter of the tube and ρ_L and ρ_G are the liquid and gas densities, respectively. p is the absolute pressure and $\dot{m}_L$ is the liquid mass velocity (mass flow rate per unit cross-sectional area). For $U_G^* \geqslant 0.4$, as the gas flow rate increases, the pressure gradient *decreases* with increasing gas flow rate (the liquid flow rate being constant) due to the decreasing intensity of the gas–liquid interaction. Eventually, the pressure gradient begins to increase again as annular flow is entered. This behaviour is characteristic of churn flow and, as will be seen, is very different from that observed in annular flow.

2. The flow mechanism in churn flow was established in the visualisation tests of Hewitt et al. (1985). In those experiments, photochromic dye tracing was used and, by matching the refractive index of the tube wall and the liquid phase, it was possible to get simultaneous visualisation of the interface and of the instantaneous velocity profile. The liquid is transported upwards in large waves which pick up liquid from a falling film ahead of them and shed liquid which forms a falling film behind them. The flow mechanism suggested by Hewitt et al. (1985) is illustrated in Fig. 2. The origin of the large waves is similar to those which cause the 'flooding' phenomenon in

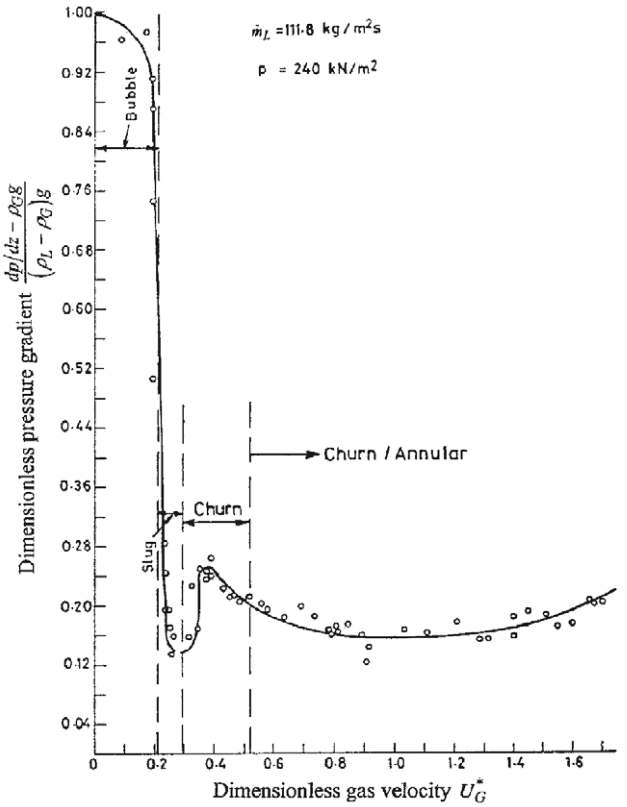

Fig. 1. An illustration of the pressure gradient distribution against dimensionless gas velocity for gas–liquid flow in vertical pipes (Owen, 1986).

countercurrent gas–liquid flow. It is perhaps helpful here to review measurements which were made by Govan et al. (1991). In these experiments, liquid was injected through an inlet sinter (section of porous wall tubing) and then removed through an outlet sinter located at a distance L below the inlet sinter. Gas entered at the bottom of the test section and passed up the tube, the gas flow being fully developed before it met the liquid (this is an important point; quite different results are obtained if the gas flow is not developed). Flooding occurs in this situation by the formation of a single wave near the outlet sinter which is then transported upwards by the gas phase and passes beyond the inlet sinter and into the upper part of the channel. After this point, part of the liquid flows upwards from the injection point and part of it flows downwards. Govan et al. (1991) compared the pressure gradient and hold-up in the region above the liquid injector both with and without the falling liquid film below the injector. They proved that no significant difference exists between the two cases. Thus, the transition to churn flow is characterised by the capability of forming flooding-type waves and there is an intimate connection between the flooding phenomenon and the existence of churn flow. In fact, flooding within the Taylor bubble in slug flow is the most likely explanation of the slug-churn transition (Jayanti and Hewitt, 1992; Jayanti et al., 1993).

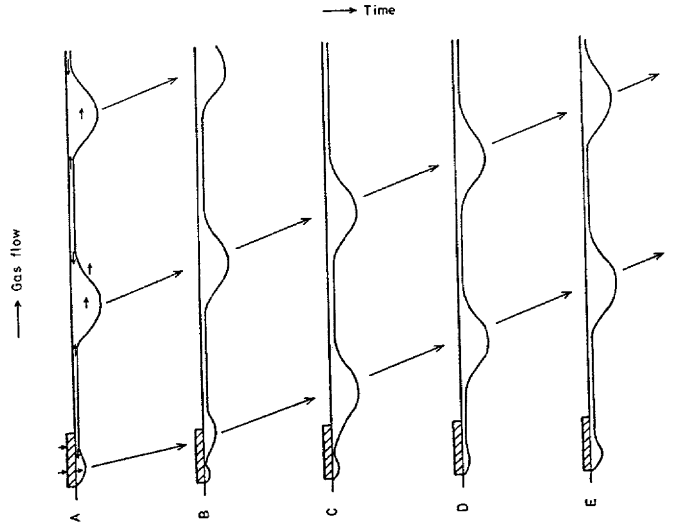

Fig. 2. Postulated mechanism of churn flow (Hewitt et al., 1985).

3. The large flooding waves are broken up to form droplets as they pass along the channel and a reasonably large fraction of the liquid can be entrained as droplets. Fig. 3 shows results obtained by Wallis (1962) which shows that the entrained fraction decreases with increasing gas velocity in what is clearly churn flow to a minimum value before *increasing* again in annular flow. In downwards co-current flow, the flooding type waves are not formed and the entrained fraction goes smoothly to zero as gas flow rate is decreased.

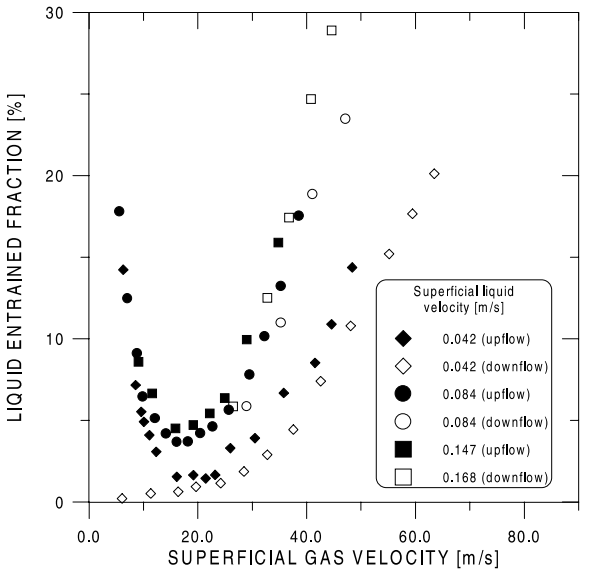

Fig. 3. Comparison of entrained fraction in upwards and downwards co-current annular flow (Wallis, 1962).

The above features of churn flow are ones which make the regime very distinct from annular flow, hence the need for a separate designation.

Although a large amount of work has been done in detailed characterisation of annular flow, there has been relatively little on churn flow. The objective of this paper is to present experimental and modelling work on the churn flow regime. The experiments were carried out at the Harwell Laboratory in the late 1980s; some preliminary results were presented in a conference paper (Govan et al., 1990) and further details are given in the thesis by Govan (1990). This work used special visualisation methods (namely a transparent liquid injector) to observe the formation of the waves in churn flow and their translation along the channel after formation. On the basis of these observations, it has been possible to develop an approximate analytical model which is consistent with the results.

In what follows, Section 2 describes the experimental arrangement, procedure and experimental results. The approximate model is presented in Section 3 together with the associated predictions. Finally, conclusions are drawn in Section 4.

2. Experiments

2.1. Experimental arrangement and procedure

In order to observe the flow behaviour close to the liquid inlet, a test section was constructed as shown in Fig. 4. Visualisation of events near the liquid entry point were made possible due to the use of a transparent liquid injector. This consisted of a length of plastic tubing through which a large number of holes were drilled, giving a smooth liquid entry analogous to that produced by a porous wall. Initial attempts used fluorinated ethylene propylene (FEP) tubing because this has a refractive index (1.34) close to that of water (1.33) thus minimizing distortion. However, the wetting characteristics of FEP are very poor and it was found to be almost impossible to create a falling film, the liquid tending instead to flow as rivulets. Attempts to improve the wetting by coating the tube also failed, and it was decided to use acrylic resin tubing similar to that used in the flooding experiments by Govan et al. (1991). This has much better wetting behaviour but a less well-matched refractive index (1.5).

Air from the site mains is measured using a standard orifice plate and fed to the bottom of the test section. Water from a stock-tank is measured using a variable-area flowmeter and pumped into a transparent parallel-sided casing surrounding the inlet section. This inlet section consists of 506 holes, nominally 0.8 mm diameter, arranged in 11 rows to give a 25 mm inlet length. The pitch of the holes is approximately 2.2 mm. Liquid entering this inlet section may leave the system by two routes:

1. It may flow upwards and pass into the main rig separator after leaving the test section.
2. It may flow *downwards*, being removed by an outlet sintered section (see Fig. 4).

The air removal from the outlet sinter (removing the down-falling liquid) was minimised using valve V1, and the test section pressure was maintained at 1.33 bar using valve V2.

The experimental procedure was as follows: the air flow was started at the desired value and then liquid passed into the transparent injection device at a low flow rate. Under these circumstances the liquid passed downwards as a falling film (countercurrent to the gas flow rate) and

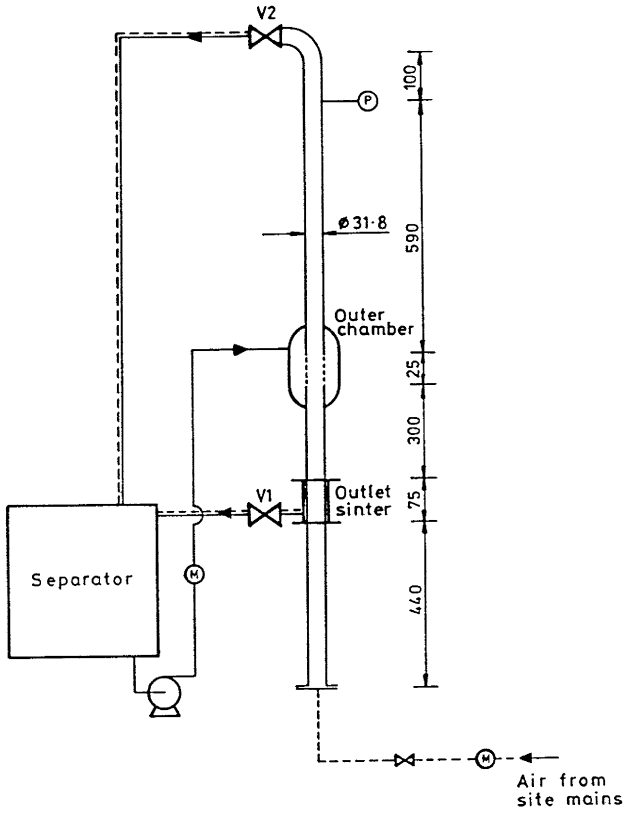

Fig. 4. Experimental arrangement used in the visualisation study.

passed out of the system through the outlet sinter. The gas flow rate was then increased until flooding occurred. A large wave was formed near the outlet sinter, was transported upwards by the gas and initiated churn flow in the upper part of the section. Waves were then repeatedly formed in the region of the liquid inlet and could be observed clearly. Liquid continued to flow downwards but this liquid was now in a sub-flooded state (Govan et al., 1991). Thus, there are essentially two regions, one above the injector which is in churn flow and one below the injector which is of falling film flow with a countercurrent gas flow. The downward flow rate was estimated from the downwards flow curve produced by Govan et al. (1991), allowing the upward flow rate to be estimated.

Flow rates from 0.027 to 0.108 kg/s of water and 0.0036 to 0.0083 kg/s of air were used (5 runs in total) and in each case the flow behaviour at the water inlet was recorded using an Ektapro high-speed video camera (1000 frames/s), the test section being illuminated from behind. By counting the number of waves over a measured time period (given by the superimposed time signal in the video frame), it is a simple matter to calculate the average wave frequency. To measure wave velocities, the video player was linked to a microcomputer equipped with a PC VisionPlus Frame Grabber. Using software written at Harwell, the position of a chosen wave may be recorded as a function of time. The results of these measurements are discussed in Section 2.2.

2.2. Experimental results

2.2.1. Visualisation

The wave formation process in churn flow is shown very clearly in the high-speed videos. The sequence of events, shown in Fig. 5, is as follows, at $t = 0$ the film immediately above the porous-wall section is flowing downwards and a wave is starting to grow at the bottom of the porous section. At $t = 12$ ms this wave is close to its maximum amplitude and soon starts to travel upwards ($t = 20$ ms). There appears to be a lot of entrainment associated with the wave (though much of this subsequently redeposits) and this shows a darker area around 25 mm above the porous section at $t = 36$ ms. At $t = 36$ ms the wave has almost disappeared from the top of the frame, and a new wave is starting to form at the inlet section.

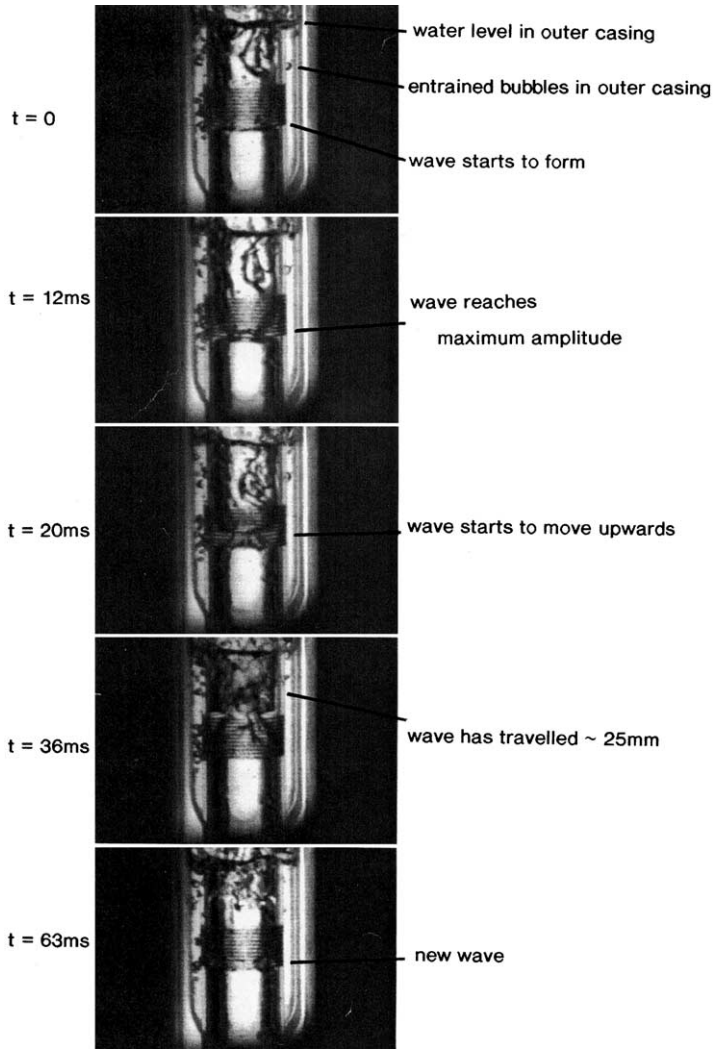

Fig. 5. Wave formation process (from Sequence 5).

It was found that at high gas/low liquid flows the process of wave formation is very regular and periodic, but becomes markedly less so as the gas flow is reduced. An example of a more chaotic behaviour is shown in Fig. 6. Here, the wave starts to grow at the bottom of the porous section but, because of the low gas flow/high liquid downflow, the wave moves slightly down the test section and grows very large ($t = 77$ ms). By $t = 133$ ms the gas flow has started to transport the wave upwards but the wave has become very distorted. At $t = 151$ ms the wave is clearly travelling upwards but the film below the inlet is still very disturbed. By $t = 235$ ms the falling film has largely returned to normal and a new wave is growing.

It will be seen, therefore, that the processes occurring are in general agreement with the mechanisms postulated by Hewitt et al. (1985) and illustrated in Fig. 2.

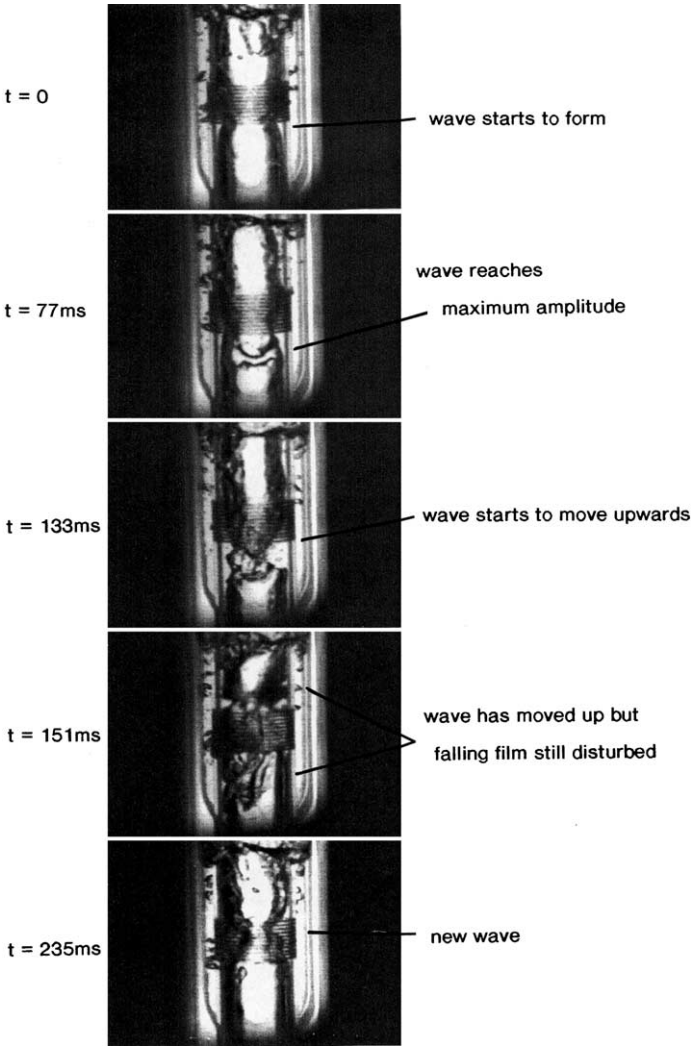

Fig. 6. Example of chaotic behaviour (from Sequence 4).

2.2.2. Wave frequencies and velocities

Table 1 shows the flow rates used in the visualisation experiments, together with the mean wave frequencies calculated from the video recordings. Note that individual waves show considerable variations about the mean, especially at high liquid/low gas flows. As expected, the wave frequency increases with increasing liquid flow (because the waves grow more quickly) and with increasing gas flow (because the critical amplitude is less and thus achieved more quickly). However, the effect is rather small in both cases.

It is also instructive to consider the average liquid flow *per wave*. The liquid upflow rate was calculated from the measurements of Govan et al. (1991) (extrapolation was necessary for Sequences 4 and 5), and the upflow per wave is obtained simply by dividing by the frequency.

For Sequence 1, though flooding has occurred, the downflow rate equals the injection rate. This is because the waves lose all their water above the injector, eventually reducing to zero amplitude. Thus, there exists a 'hanging film' above the injector in which transport up by the waves is exactly balanced by the drainage effect; Sequence 2 results are obviously influenced in the same way. In the hanging film region, no net upflow occurs and all of the liquid enters the falling film region below the injector. However, for the results from Sequences 3–5, the net liquid transported per wave is roughly constant.

Hewitt et al. (1985) made measurements of wave frequencies, velocities and amplitudes in air–trichloroethylene churn–annular flows at atmospheric pressure in a 10-mm diameter test section. The wave frequencies and velocities are compared with those from the present experiments in Figs. 7 and 8. The results are plotted against the gas mass velocity, i.e., the mass flow rate divided by the cross-sectional area of the pipe. The results are seen to be broadly consistent, but the measurements of Hewitt et al. show a strong effect of liquid mass velocity, both frequency and velocity being considerably higher at the highest liquid flow rate. This effect seems to be absent in the present data; this may be a result of the differing physical properties or may reflect the fact that in small diameter tubes the liquid phase may occupy a significant volume in the pipe, thus increasing the gas velocity.

Table 1
Wave frequencies and velocities from visualisation experiments

No. of video sequence	$\dot{M}_G \times 10^{-3}$ (kg/s)		U_G (m/s)	$\dot{M}_L \times 10^{-3}$ (kg/s)	$\dot{M}_{LU} \times 10^{-3}$ (kg/s)
1	8.3		6.5	27	–
2	8.3		6.5	42	7
3	6.8		5.3	103	51
4	4.5		3.5	105	32
5	3.6		2.8	108	27
No. of video sequence	Total time	No. of waves	Frequency (Hz)	Net upflow per wave $\times 10^{-3}$ (kg)	Wave velocity (m/s)
1	3305	41	12.4	–	0.46
2	4895	65	13.3	0.5	1.34
3	4904	78	15.9	3.2	0.75
4	5008	52	10.4	3.1	0.70
5	5498	54	9.8	2.8	0.52

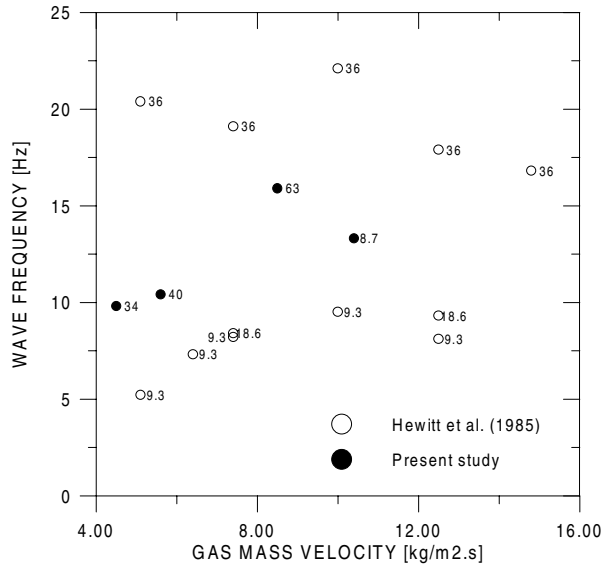

Fig. 7. Comparison of wave frequency with data of Hewitt et al. (1985).

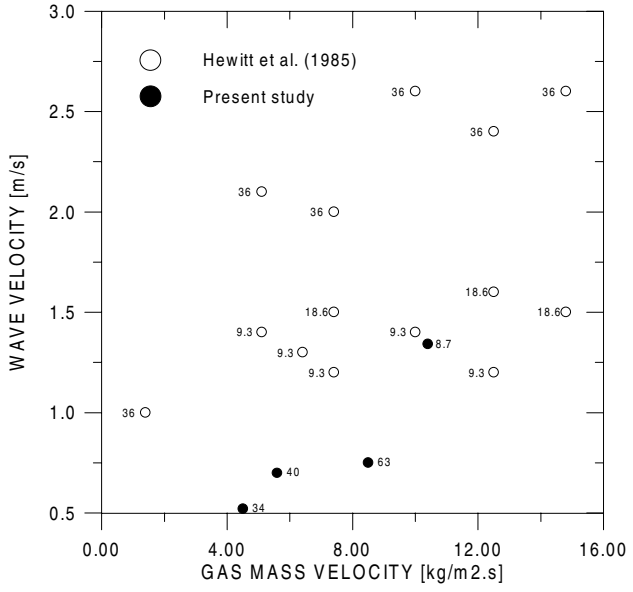

Fig. 8. Comparison of wave velocities with data of Hewitt et al. (1985).

2.2.3. Distance travelled by the waves

Fig. 9 shows typical measurements of wave position (relative to the bottom of the porous section where the waves generally form) versus time from the start of the growth of the wave.

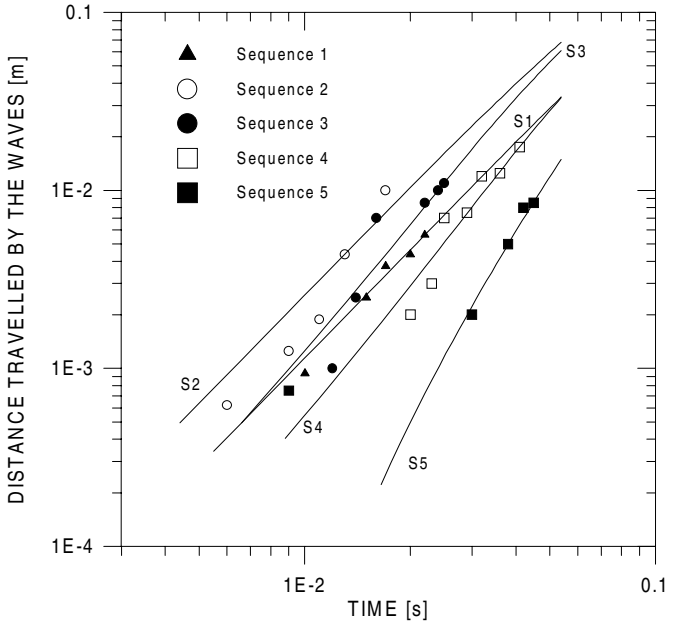

Fig. 9. Wave position versus time.

With exception of the wave measured in Sequence 1, whose behaviour is rather anomalous, the measurements are very consistent, they show that as the gas velocity is decreased the growth/acceleration period is longer and the mean velocity is lower, as would be expected. Values of the mean velocity are given in Table 1 and compared with the gas superficial velocity. With the exception of Sequence 1, the wave velocity is around 20% of the superficial gas velocity.

3. The theoretical model

The model for wave growth is based on macroscopic balances of mass and momentum over a control volume which encompasses the wave. The wave is assumed to be coherent around the periphery of the pipe.

3.1. Conservation principles

Fig. 10 illustrates the geometry of the problem. It has been experimentally observed that the waves generally grow at the bottom of the porous section before start moving upwards. There is a falling film downstream (above) to the wave and liquid is shed by the wave as it grows. If the mass flow rates entering, $\dot{M}_{\mathrm{LF,in}}$, and leaving, $\dot{M}_{\mathrm{LF,out}}$, the wave are such that,

$$\dot{M}_{\mathrm{LF,out}} < \dot{M}_{\mathrm{LF,in}}, \tag{2}$$

then there will be mass storage in the control volume and the wave will grow. The wave will move upwards when it reaches a critical size and the net force acting on it is directed upwards.

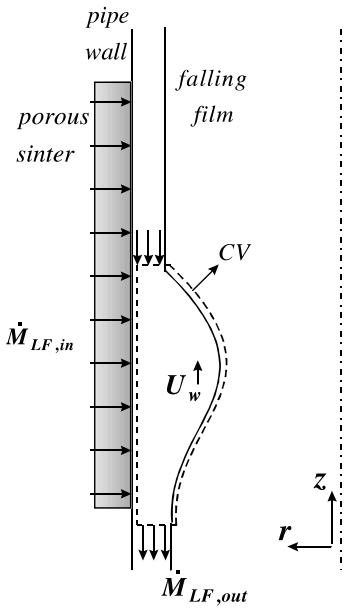

Fig. 10. An illustration of the problem geometry.

A primary assumption of the macroscopic model is that the control volume encompassing the wave moves with velocity U_w relative to a fixed frame of reference. An application of the mass and momentum conservation principles is carried out as follows:

$$\rho_L \frac{d}{dt} V_w = \dot{M}_{LF,in} - \dot{M}_{LF,out} \tag{3}$$

and

$$\sum F_z = \rho_L \frac{d}{dt}(U_w V_w) - U_{LF,in}\dot{M}_{LF,in} + U_{LF,out}\dot{M}_{LF,out}, \tag{4}$$

where V_w is the wave volume and $U_{LF,in}$ and $U_{LF,out}$ are the mean liquid film velocities in and out of the control volume. ρ_L is the liquid density, t is the time and $\sum F_z$ is the resultant force acting on the wave in the axial direction, z.

Eqs. (3) and (4) can be solved provided that V_w and $\sum F_z$ are known. The wave volume is calculated by assuming that the shape of the wave is known and the resultant force is estimated through a force balance. These calculations are described in the following sections.

3.2. Wave shape and volumetric relationships

Direct calculation of the detailed shape of the large waves in churn flow may not be currently feasible. Thus, in any analysis, it is necessary to assume a shape. As was mentioned above, the waves are related to those formed in flooding; viable analyses of flooding have been performed by McQuillan et al. (1985) and Costigan (1997) based on the assumption that the waves are hemi-

spherical in form. However, it is unlikely that the waves would be of hemispherical shape; in an analysis of wave growth associated with flooding, Shearer and Davidson (1965) calculated a shape based on a force balance. The wave was somewhat asymmetric in form but it is not known whether waves in the developed churn flow region would have the same form (the Shearer and Davidson analysis was based on a stationary wave). In fact, Hewitt et al. (1985) measured wave shapes based on the visualisation experiments and compared them with the shape calculated by Shearer and Davidson. Though there was considerable variation between the wave shapes, they clearly did not conform either to the shape predicted for the stationary wave by Shearer and Davidson or to the hemispherical shape assumed by McQuillan et al. and Costigan. In the present analysis, therefore, it has been assumed that the wave is *sinusoidal* in shape. This is reasonably consistent with the results of Hewitt et al. (1985) and is considered to be a better approximation than assuming a hemispherical shape. However, since the assumption of a hemispherical shape gives reasonable answers for flooding, it is not considered that the exact shape is significant in governing the qualitative results from the analysis.

It is assumed that the shape of the wave is known and that this shape is retained as the wave grows. The thickness of the liquid film in wave region, δ_w, is given by (see Fig. 11),

$$\delta_w(z) = \begin{cases} \delta_{w1}, & 0 \leqslant z \leqslant L_w/2, \\ \delta_{w2}, & L_w/2 \leqslant z \leqslant L_w, \end{cases} \tag{5}$$

where

$$\delta_{w1} = \frac{1}{2}\left[(A_w + \delta_{s,out}) + (A_w - \delta_{s,out})\cos\frac{2\pi(L_w/2 - z)}{L_w}\right] \tag{6}$$

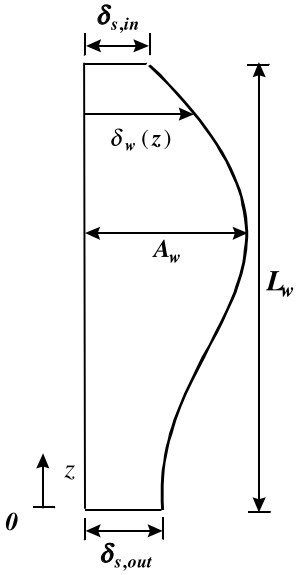

Fig. 11. The assumed geometry of the wave.

and

$$\delta_{w2} = \frac{1}{2}\left[(A_w + \delta_{s,in}) - (A_w - \delta_{s,in})\cos\frac{2\pi(L_w - z)}{L_w}\right]. \tag{7}$$

In Eqs. (5)–(7), L_w is the length of the wave, A_w is the wave amplitude and $\delta_{s,in}$ and $\delta_{s,out}$ are the thicknesses of the liquid film at the top ($z = L_w$) and bottom ($z = 0$) of the wave, respectively. The wave volume is given by

$$V_w = \pi d_T\left[\int_0^{L_w/2}\delta_{w1}(z)\,dz + \int_{L_w/2}^{L_w}\delta_{w2}(z)\,dz\right]. \tag{8}$$

Integration of Eq. (8) gives

$$V_w = \frac{1}{4}\pi d_T L_w(2A_w + \delta_{s,in} + \delta_{s,out}). \tag{9}$$

The time derivative of the wave volume is calculated assuming that L_w is approximately constant. Thus,

$$\frac{d}{dt}V_w = \frac{1}{4}\pi d_T L_w\left(2\frac{d}{dt}A_w + \frac{d}{dt}\delta_{s,in} + \frac{d}{dt}\delta_{s,out}\right). \tag{10}$$

As the wave moves upwards along the sintered section (i.e., the porous wall section over which the liquid is introduced), the values of $\dot{M}_{LF,in}$ and $\dot{M}_{LF,out}$ are likely to vary with distance. At one extreme *all* the liquid flowing into the injection region will enter the wave which is initially stationary at the bottom of the injector region; some of this liquid flows out from the bottom of the wave to form the downward falling film, but this is accounted for in the model. When the wave is transported to a position just above the top of the injector region, then *none* of the liquid entering the injector passes into the wave. An exact prediction of the amount of liquid entering the wave in between these two extreme conditions is difficult and a simple assumption is made that the amount of the liquid entering the injector which goes into a wave will depend linearly on the position of the wave in the injector region. It is not believed that this assumption affects the analysis materially. Fig. 12 illustrates the variation of $\dot{M}_{LF,in}$ and $\dot{M}_{LF,out}$ with distance as the wave travels upwards along the sintered section. The idealised curves are as follows:

$$\dot{M}_{LF,in}(z) = \left(\dot{M}_L - \dot{M}_{LE}\right) - \frac{\left[\left(\dot{M}_L - \dot{M}_{LE}\right) - \dot{M}_{LF,ss}\right]z}{L_{sint}} \tag{11}$$

and

$$\dot{M}_{LF,out}(z) = \dot{M}_{LF,out}(0) - \frac{\left[\dot{M}_{LF,out}(0) - \dot{M}_{LF,ss}\right]z}{L_{sint}}, \tag{12}$$

where $\dot{M}_L$ is the total liquid flow rate, L_{sint} is the length of the sintered section, $\dot{M}_{LE}$ is the mass flow rate of entrained liquid and $\dot{M}_{LF,ss}$ is the flow rate in the falling film region between waves attained towards the end of the sintered section, where some sort of steady state is reached. The true value

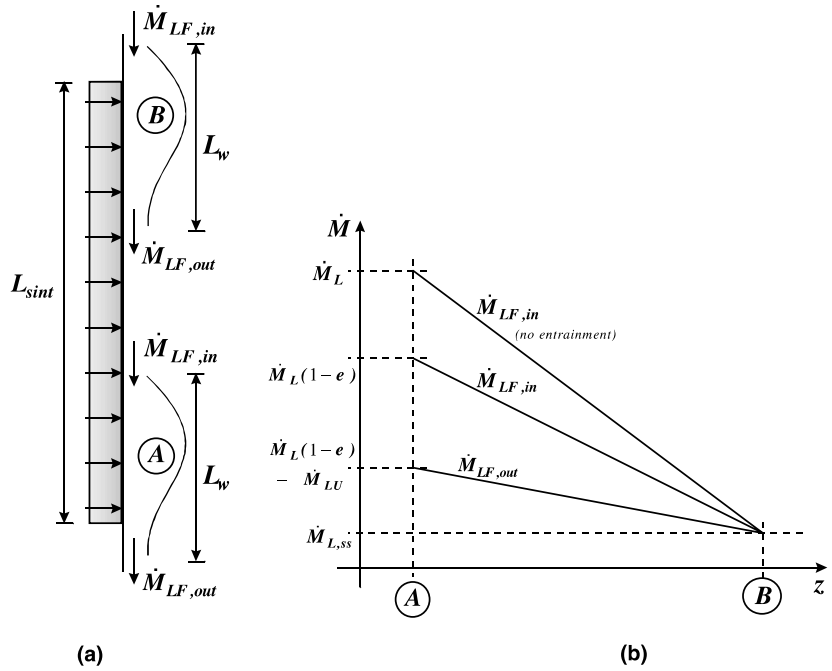

Fig. 12. Illustration and model of flow rates in and out of the wave.

of $\dot{M}_{\mathrm{LF,ss}}$ is not known, however calculations with values of $\dot{M}_{\mathrm{LF,ss}}$ ranging from 5% to 15% of $\dot{M}_{\mathrm{L}}$ were carried out without causing any significant changes to the final results.

$\delta_{\mathrm{s,in}}$ and $\delta_{\mathrm{s,out}}$, are calculated via the Nusselt film theory,

$$\delta_{\mathrm{s}} = \left[\frac{3\eta_{\mathrm{L}}\dot{M}_{\mathrm{LF}}}{\pi d_{\mathrm{T}}\rho_{\mathrm{L}} g(\rho_{\mathrm{L}} - \rho_{\mathrm{C}})} \right]^{1/3}, \tag{13}$$

where $\dot{M}_{\mathrm{LF}}$ is the film flow rate in or out of the wave in a fixed frame of reference. η_{L} is the liquid kinematic viscosity and ρ_{C} is the core density, defined in Section 3.3.

In the experiments of Hewitt and Wallis (1963) film thickness measurements in countercurrent flow showed that the mean film thickness agreed closely with the Nusselt equation.

3.3. Force balance over the coherent wave

The balance of forces on the wave is schematically shown in Fig. 13. The analysis is based on that of Shearer and Davidson (1965), the main difference being that the shape of the wave is known a priori in the present simulation and is not the dependent variable as in Shearer and Davidson's calculation. A similar approach was also adopted by Hewitt et al. (1985) and McQuillan et al. (1985). The forces are as follows:

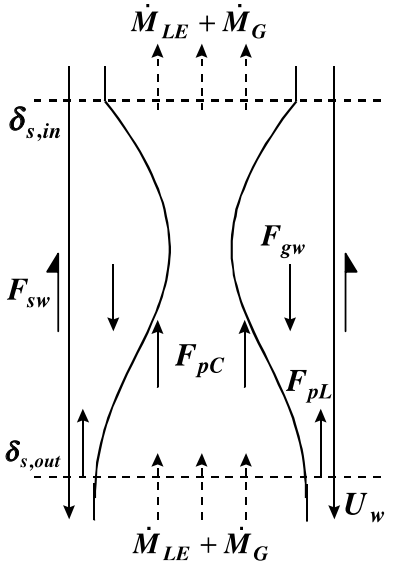

Fig. 13. Force balance over a coherent wave.

1. *Gravitational force*. F_{gw} is due to the action of the gravitational field on the mass of liquid that forms the wave.

$$F_{gw} = \frac{1}{4}\pi\rho_L g d_T L_w (2A_w + \delta_{s,in} + \delta_{s,out}). \tag{14}$$

2. *Pressure force on the core*. F_{pC} is due to the pressure unbalance over the wave in the core side (separation at the leeward side of the wave).

$$F_{pC} = \frac{2\pi\rho_C}{(d_T - 2A_w)^4}(U_C - U_w)^2(d_T - 2\delta_{s,out})^2(A_w - \delta_{s,out})^2(A_w + \delta_{s,out} - d_T)^2. \tag{15}$$

The above equation was derived by applying the Bernoulli equation to the flow in the core region, where it is assumed (Shearer and Davidson, 1965) that the pressure at the leeward side of the wave remains equal to its value at the wave crest. F_{pC} also accounts for the (opposite) force caused by the change in core velocity over the control volume as one assumes that the streamlines remain parallel downstream to the crest plane. ρ_C and U_C are the homogeneous core density and velocity, respectively. They are calculated assuming a homogeneous flow of gas and entrained droplets (if any) in the core. These are given by

$$\rho_C = \frac{\dot{m}_{LE} + \dot{m}_G}{(\dot{m}_{LE}/\rho_L) + (\dot{m}_G/\rho_G)} \tag{16}$$

and

$$U_C = \frac{(\dot{m}_{LE}/\rho_L) + (\dot{m}_G/\rho_G)}{(1 - (2\delta_s/d_T))^2}. \tag{17}$$

In Eqs. (16) and (17), $\dot{m}_{LE}$ and $\dot{m}_G$ are the entrained liquid and gas mass velocities.

For consistency in the pressure calculations, U_C is always evaluated using $\delta_s = \delta_{s,out}$.

3. *Pressure force on the liquid*. F_{pL} is due to a pressure unbalance at the top and at the bottom of the wave on the liquid film. The magnitude of F_{pL} is given by

$$| F_{pL} | = | p_{L,in} A_{LF,in} - p_{L,out} A_{LF,out} |, \tag{18}$$

where $A_{LF,in}$ and $A_{LF,out}$ are the cross-sectional area of the liquid film at the planes $z = L_w$ and $z = 0$, respectively. $p_{L,in}$ and $p_{L,out}$ are the pressures acting normal to these planes in the liquid film.

A simplification to Eq. (18) is carried out as follows:

$$p_{L,in} A_{LF,in} - p_{L,out} A_{LF,out} \cong (p_{L,in} - p_{L,out}) \overline{A}_{LF}, \tag{19}$$

where $\overline{A}_{LF}$ is an average falling film area given by

$$\overline{A}_{LF} = \frac{\pi}{2} d_T (\delta_{s,in} + \delta_{s,out}). \tag{20}$$

The pressure difference between the top and bottom of the wave on the liquid side is given by

$$p_{L,in} - p_{L,out} = p_{C,in} - p_{C,out} + \sigma \left(\left. \frac{d^2 \delta_s}{dz^2} \right|_{z=0} - \left. \frac{d^2 \delta_s}{dz^2} \right|_{z=L_w} \right), \tag{21}$$

where σ is the surface tension. The pressure drop in the core side, $p_{C,in} - p_{C,out}$, is given by the same analysis which led to the calculation of F_{pC}

$$p_{C,in} - p_{C,out} = \frac{8 \rho_C}{(d_T - 2A_w)^4} (A_w - \delta_{s,out})^2 (U_C - U_w)^2 (A_w + \delta_{s,out} - d_T)^2 \tag{22}$$

and

$$\left(\left. \frac{d^2 \delta_s}{dz^2} \right|_{z=0} - \left. \frac{d^2 \delta_s}{dz^2} \right|_{z=L_w} \right) = \frac{2\pi^2}{L_w^2} (\delta_{s,out} - \delta_{s,in}). \tag{23}$$

F_{pL} is finally given by

$$F_{pL} = (p_{L,out} - p_{L,in}) \overline{A}_{LF}. \tag{24}$$

4. *Wall shear force*. To calculate the force due to shear stress at the wall in the wave region, the approach taken by Hewitt et al. (1985) based on studies on slug flows (Maron and Brauner, 1982) and on inclined wavy falling film flows (Brauner et al., 1985) was adopted and it is illustrated in Fig. 14. The incoming fluid is brought to rest (with respect to the wave) in a mixing zone after which a new boundary layer is formed on the (moving) wall as illustrated. Assuming that the mixing zone is short, the boundary layer length may be taken as approximately equal to the wave region length. Thus, assuming the boundary layer to be laminar, the frictional force (in this case downwards with respect to the wave) can be calculated from the standard boundary layer expression,

$$F_{sw} = \left(\frac{8 \rho_L L_w U_w \eta_L}{15} \right)^{1/2}. \tag{25}$$

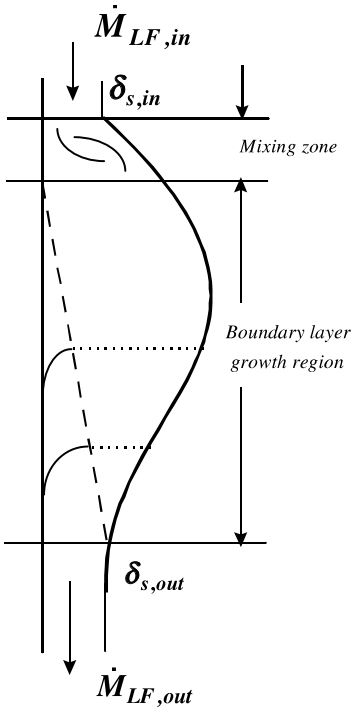

Fig. 14. The boundary layer hypothesis for wall shear stress.

Visual observation of the velocity profile in the wave region by Hewitt et al. (1985) showed that the actual movement of the liquid in this region does not conform to this pattern. In fact, there is a strong liquid circulation which gives rise to a peak in the velocity profile. However, at the level of sophistication of the present methodology, where numerous simplifying assumptions were made, it is believed that a more realistic, and therefore more complicated, representation of the liquid velocity distribution in the wave region will not lead to a significant improvement of the results.

5. *Interfacial shear force*. The shear force exerted on the liquid surface by the gas flow is neglected. Shearer and Davidson (1965) performed an order-of-magnitude calculation that showed a much greater influence of normal pressure forces. There is an evidence that suggests that the interfacial shear stress is small compared with the gravitational force up to the point where flooding waves are generated; thus, in the experiments of Hewitt and Wallis (1963) there was little or no effect on mean film thickness as the gas velocity was increased from zero up to just before that required for flooding. However, the importance of shear stress once the wave is formed and is being transported cannot easily be deduced either from the Shearer and Davidson (1965) order-of-magnitude calculation or from the observations of Hewitt and Wallis (1963). In order to calculate the shear force, it is necessary to have recourse to computational fluid dynamics (CFD) calculations and such calculations on flooding-type waves are reported by Jayanti et al. (1996). Their calculations show that the shear force on the wave is of the order of 20% of the pressure force. Since it is difficult to estimate the shear force without recourse to CFD, and since it is a

relatively small proportion of the total force, it has been neglected in the current analysis. Note that the nature of flooding waves is different from that of disturbance waves characteristic of co-current annular flows. In the latter, interfacial shear plays a dominant role whereas pressure forces may by neglected.

The net force acting on the wave is thus

$$\sum F_z = F_{pC} + F_{pL} - F_{sw} - F_{gw}. \tag{26}$$

3.4. Solution of conservation equations

After combination of wave volumetric relationships, Eqs. (9) and (10), with Eqs. (3) and (4), the conservation principles can be written as

$$\frac{d}{dt}A_w = 2\frac{\dot{M}_{LF,in} - \dot{M}_{LF,out}}{\pi\rho_L d_T L_w} - \frac{U_w}{6L_{sint}}\left[\frac{\delta_{s,in}\left(\dot{M}_{LF,ss} + \dot{M}_{LE} - \dot{M}_L\right)}{\dot{M}_{LF,in}} + \frac{\delta_{s,out}\left(\dot{M}_{LF,ss} - \dot{M}_{LF,out}(0)\right)}{\dot{M}_{LF,out}}\right] \tag{27}$$

and

$$\frac{d}{dt}U_w = 4\left\{\left\{\sum F_z + \frac{\dot{M}^2_{LF,out}}{\pi d_T \rho_L \delta_{s,out}} - \frac{\dot{M}^2_{LF,in}}{\pi d_T \rho_L \delta_{s,in}}\right\} \Big/ \left\{\pi\rho_L d_T L_w (2A_w + \delta_{s,in} + \delta_{s,out})\right\}\right\}. \tag{28}$$

The distance travelled by the wave is given by

$$\frac{d}{dt}z = U_w. \tag{29}$$

Eqs. (27)–(29) are solved using a fourth-order Runge–Kutta method (Press et al., 1992) with the following initial conditions:

$$A_w(0) = A_{w,crit}, \tag{30}$$

$$U_w(0) = 0, \tag{31}$$

$$z(0) = 0, \tag{32}$$

where $A_{w,crit}$ is the critical wave amplitude, i.e., the amplitude at which the wave starts moving upwards. At this critical condition, the sum of forces acting on the wave is equal to zero. The resultant force is calculated applying an analysis similar to that by Costigan (1997).

The solution procedure of the mathematical model is as follows. $\dot{M}_{LF,in}$ is set equal to $\dot{M}_L(1-e)$, where e is the fraction of liquid entrained as droplets. e is not known a priori and it is assumed constant. L_w and $\dot{M}_{LF,out}(0)$ are also not previously known. Therefore, $L_w, \dot{M}_{LF,out}(0)$ and e are set to vary over a wide range of values and at each iteration the system of equations (28), (29) is solved giving distributions of wave amplitude, velocity and distance travelled as a function of time. The set of parameters corresponding to the chosen solution is the one whose distribution gives the smallest deviation to the experimental data on the distance travelled by the wave.

For all conditions observed, the ranges of values assessed are as follows: $L_w, d_T/6$–d_T; $\dot{M}_{LF,out}(0)$, 0–$(\dot{M}_L - \dot{M}_{LU})(1-e)$; and e, 0–0.25. $\dot{M}_{LU}$ is the flow rate of liquid carried upwards.

3.5. Analytical results

The values of critical wave amplitude, liquid entrained fraction and wave parameters that give the best fit to the experimental data for each sequence are summarised in Table 2. Also shown is the mean error, E, associated with the prediction for each sequence defined as

$$E = \frac{1}{N}\sum_{i=1}^{N}\frac{|\, z_{pred,i} - z_{exp,i}\,|}{z_{exp,i}}, \tag{33}$$

where N is the number of experimental points available for each sequence. z_{pred} and z_{exp} are the predicted and experimental axial distances travelled by the wave.

It can be seen from Table 2 that both the length of the wave, L_w, and the critical amplitude, $A_{w,crit}$, increase with decreasing gas flow rate at constant liquid flow rate (Sequences 3–5) and with increasing liquid flow rate at constant gas flow rate (Sequences 1 and 2). This is consistent with what has been observed experimentally. By comparing the values of liquid flow rate out of the wave, $\dot{M}_{LF,out}(0)$, for Sequences 3–5, it can be observed that the mass storage in the control volume is higher for the higher gas flow rates. Therefore, the rate of growth is higher for such cases and the wave critical amplitude is attained more rapidly. Also shown in Table 2 are the values of wave velocity at the end of the sinter ($z = 25$ mm) for each experimental sequence. With exception of Sequence 2, the agreement between these values and the mean velocities obtained experimentally is not so good. However, the range of predicted velocities is not inconsistent when compared to that obtained by Hewitt et al. (1985) for both air–water and air–trichlorethylene flows. The predicted entrained fraction remains approximately constant throughout the assessed range of parameters; though a small gas flow rate effect is picked up in Sequences 3–5.

The solid lines in Fig. 9 correspond to the predictions of distance travelled by the waves for each one of the sequences (S1–S5). The general trend of the experimental data is generally well picked up by the methodology (with exception of Sequence 2). Fig. 15 shows the calculated wave velocity distributions for each sequence. It can be observed that the wave of Sequence 5 has a slight negative velocity before starting to move upwards.

Table 2
Results obtained using the mathematical model

Sequence no.	$A_{w,crit}$ (mm)	e (–)	$\dot{M}_{LF,out}(0) \times 10^{-3}$ (kg/s)	L_w (mm)	Wave velocity (m/s)	E (%)
1	4.08	0.06	14.4	9.8	1.06	12.7
2	4.09	0.07	24.4	10.8	1.44	34.4
3	3.89	0.10	44.9	10.5	1.69	23.8
4	4.76	0.10	62.4	13.5	1.20	19.7
5	5.30	0.08	70.4	14.3	0.81	25.3

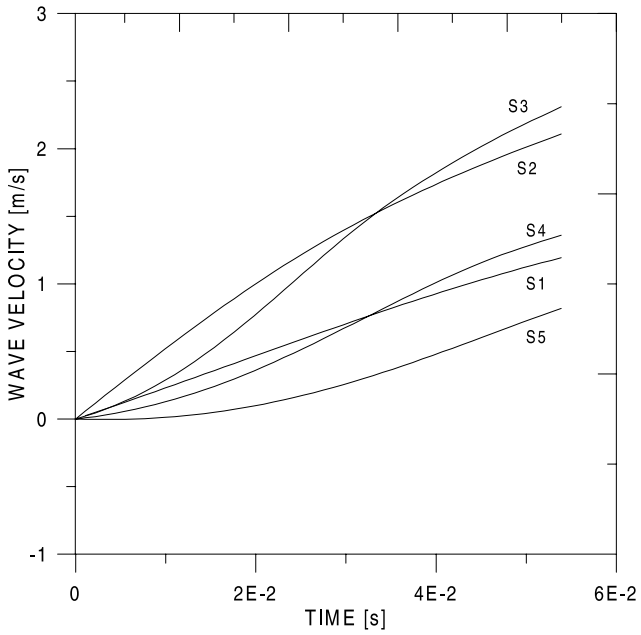

Fig. 15. Calculated wave velocity distribution.

4. Conclusions

The present work has dealt with experimental and modelling work on churn flow of an air–water mixture in a vertical pipe. High-speed video photography has been used to study the behaviour of the flow close to the liquid inlet in a specially constructed transparent porous-wall test section. The main conclusions arising from this study are as follows:

1. The video recordings showed clearly the process of wave formation in churn flow which, in this case was co-existing with a falling film below the injector. The observed mechanism was in general agreement with that postulated by Hewitt et al. (1985) and illustrated in Fig. 2.

2. Measurements of wave frequencies and velocities from the video recordings gave results which were broadly consistent with the previous results of Hewitt et al. (1985), but showing much weaker effects of liquid flow rate.

3. A simple model to describe the wave levitation process was proposed. The model considers the formation and growth of waves, taking account of the forces on the waves due to gravity, the resolved normal force due to gas flow over the wave, and wall shear forces. The model is calibrated against measurements of the location of the waves as a function of time. Reasonably self-consistent values are obtained for wave amplitude at the point of levitation, wave length, entrained liquid fraction and the downwards leakage rate from the wave. It should be stressed that the model does not claim to be predictive for such a complex regime as churn flow. Rather, it is aimed at giving insights into the mechanisms. The observed self-consistency supports the wave levitation and transport mechanism for this flow regime. However, prediction of the flow

phenomena in terms of just the flow rates and channel geometry remains a formidable challenge.

Acknowledgements

The authors wish to thank J. Dowling (formerly Photographic Group, Harwell) for his assistance with the video recordings, P. Lovegrove (formerly Thermal Hydraulics Division, Harwell) for his help with the rig design and Dr. C. Lawrence (Imperial College) for useful comments and suggestions to the mathematical model. The experimental work was carried out as part of the Underlying Research Programme of the United Kingdom Atomic Energy Authority. One of us (JRB) thanks the Brazilian National Research Council (CNPq – Conselho Nacional de Desenvolvimento Científico e Tecnológico) for the award of a scholarship (Grant No. 200085/97-2).

References

Brauner, N., Maron, D.M., Dukler, A.E., 1985. Modelling of wavy flow in inclined thin films in the presence of interfacial shear. Chem. Eng. Sci. 40, 923–937.

Costigan, G., 1997. Flow pattern transitions in vertical gas–liquid flows. D.Phil. Thesis, Oxford University, UK.

Govan, A.H., 1990. Modelling of vertical annular and dispersed two-phase flows. Ph.D. Thesis, University of London, Imperial College.

Govan, A.H., Hewitt, G.F., Lim, S.B., 1990. Visualisation studies of churn flow in a vertical pipe. Second Irish Research Colloquia, IChemE, Belfast, March 9.

Govan, A.H., Hewitt, G.F., Richter, H.J., Scott, A., 1991. Flooding and churn flow in vertical pipes. Int. J. Multiphase Flow 17, 27–44.

Hewitt, G.F., Wallis, G.B., 1963. Flooding and associated phenomena in falling film in a vertical tube. In: Proceedings of Multi-phase Flow Symposium, Philadelphia, PA, November 17–22, pp. 62–74.

Hewitt, G.F., Hall-Taylor, N.S., 1970. Annular Two-phase Flow. Pergamon Press, Oxford, UK.

Hewitt, G.F., Martin, C.J., Wilkes, N.S., 1985. Experimental and modelling studies of annular flow in the region between flow reversal and the pressure drop minimum. PCH Physicochem. Hydrodyn. 6, 69–86.

Jayanti, S., Hewitt, G.F., 1992. Prediction of the slug-to-churn transition in vertical two-phase flow. Int. J. Multiphase Flow 18, 847–860.

Jayanti, S., Hewitt, G.F., Low, D.E.F., Hervieu, E., 1993. Observation of flooding in the Taylor bubble of co-current upwards slug flow. Int. J. Multiphase Flow 19, 531–534.

Jayanti, S., Tokarz, A., Hewitt, G.F., 1996. Theoretical investigation of the diameter effect on flooding in countercurrent flow. Int. J. Multiphase Flow 22, 307–324.

McQuillan, K.W., Whalley, P.B., Hewitt, G.F., 1985. Flooding in vertical two-phase flow. Int. J. Multiphase Flow 11, 741–760.

Maron, D.M., Brauner, N., 1982. New thoughts on the mechanism of gas–liquid slug flow. Lett. Heat Mass Transfer 9, 333–342.

Nicklin, D.J., Davidson, J.F., 1962. The onset of instability in two-phase slug flow. In: Int. Mech. Eng. Proc. Symp. Two-phase Flow, UK, February 7, Paper No. 4.

Owen, D.G., 1986. An experimental and theoretical analysis of equilibrium annular flows. Ph.D. Thesis, University of Birmingham, UK.

Press, W.H., Teukolsky, S.A., Vetterling, W.T., Flannery, B.P., 1992. Numerical Recipes in FORTRAN – The Art of Scientific Computing, second ed. Cambridge University Press, Cambridge.

Shearer, C.J., Davidson, J.F., 1965. The investigation of a standing wave due to gas blowing upwards over a liquid film; its relation to flooding in wetted-wall columns. J. Fluid Mech. 22, 321–335.

Taitel, Y., Barnea, D., Dukler, A.E., 1980. Modelling flow pattern transition for steady upwards gas–liquid flow in vertical tubes. AIChE J. 26, 345–354.

Wallis, G.B., 1962. The onset of droplet entrainment in annular gas–liquid flow. General Electric Report No. 62 GL127.

Zuber, N., Findlay, J.A., 1965. Average volumetric concentration in two-phase flow systems. J. Heat Transfer 87, 453–468.